



Influence of the Cooling Rate on Mechanical and Corrosion Properties of Ferritic Si–Mo Ductile Cast Iron

GAETANO PALUMBO, MARCIN GÓRNY, and ADAM BITKA

In this study, the effect of the cooling rate controlled by different castings thickness ranging from 3 to 25 mm on the mechanical and corrosion behavior of Si–Mo ductile iron (DI) castings was investigated. SEM-EBSD investigations demonstrated that the nodule counts, nodularity, and ferrite phase increased while the ferritic grain size decreased with decreasing in the casting wall thickness; this in turn led to improvements in the tensile properties of the DI. The corrosion behavior of Si–Mo DI castings was investigated after different immersion times in a 3.5 wt pct NaCl solution *via* electrochemical experiments. The electrochemical results showed that the corrosion resistance of Si–Mo DI decreased in the following order: 3 > 5 > 13 > 25 mm. The results indicated that all of the tested DI samples exhibited galvanic corrosion between the nobler carbide and ferritic matrix phases. SEM analysis showed that the dissolution of the ferrite phase with the pearlite phase exposed and accumulated on the DI's surface, which led to intense corrosion acceleration. The higher corrosion rates that were observed for those samples with higher casting wall thicknesses could be associated with the higher contents of pearlite/carbide.

<https://doi.org/10.1007/s11661-023-07023-x>

© The Author(s) 2023

I. INTRODUCTION

Si–Mo ductile cast iron (Si–Mo DI) belongs to the family of high-quality and modern ductile iron of which microstructure consists of graphite spheres embedded in a metallic ferrite matrix with a small fraction of pearlite and carbides such as M_6C and Fe_2MoC .^[1] Si–Mo cast iron differs from typical ductile iron due to its higher contents of silicon (*e.g.*, 4 to 6 pct) and molybdenum (*e.g.*, 0.5 to 2.0 pct), which makes it a material resistant to oxidation to temperatures of up to 850 °C to 860 °C.^[2] The maximum pointwise temperature at full engine load may be higher than 750 °C, and the main damage mechanisms in service are high-temperature oxidation and thermo-mechanical fatigue as reported by Matteis *et al.*^[3] Combined with its reasonably low cost,

the high-temperature mechanical and high-temperature corrosion resistance properties of this material have made it very attractive in applications such as exhaust manifolds, turbine castings, and many types of elevated-temperature applications.^[1,4–12] From an economic standpoint, the manufacturing of thin-walled castings has recently gained enormous popularity. The literature reports that DI has strength-to-density and elastic modulus-to-density ratios that are similar to those castings that are made of aluminum alloys^[13–15]; therefore, it can be used to produce relatively cheap thin-wall-thickness and lightweight components with good mechanical properties (even though DI is not a light metallic alloy).^[13–15] However, the process of obtaining thin-walled castings is not simple. Górny *et al.*^[14,16] and Nofal *et al.*^[17] reported that the cooling rate strongly influenced the microstructure of the final product and its mechanical properties. It was reported that the yield stress increased after increasing the pearlite fraction, while a reduction of the spheroidal graphite fraction had an adverse effect on the tensile and fatigue of the Si–Mo DI samples.^[18,19]

DI is a multiphase material, with each phase having its own electrochemical potential. From a corrosion point of view, the weak point of such a metallurgical system is due to the formation of micro-galvanic cells between the various phases with different corrosion reactivities. These differences in potential could lead to a dissolution of the less noble ferrite matrix phase (*i.e.*,

GAETANO PALUMBO is with the Department of Chemistry and Corrosion of Metals, Faculty of Foundry Engineering, AGH University of Science and Technology, Reymonta St. 23, 30-059 Kraków, Poland. Contact e-mail: gpalumbo@agh.edu.pl MARCIN GÓRNY is with the Department of Cast Alloys and Composites Engineering, Faculty of Foundry Engineering, AGH University of Science and Technology, Reymonta St. 23, 30-059 Kraków, Poland. ADAM BITKA is with the Łukasiewicz Research Network – Foundry Research Institute, ul. Zakopiańska 73, 30-418 Kraków, Poland.

Manuscript submitted October 16, 2022; accepted February 18, 2023.

Article published online March 10, 2023

anodic site) and an accumulation of residual cementite and graphite (*i.e.*, cathodic sites). This in turn can further accelerate the corrosion rate of the metal.^[20–23] Górný *et al.* observed that thinner casting wall thicknesses increased the formation of the ferrite phase.^[14,16] Therefore, adjusting the microstructure is key for improving the corrosion resistance of the manufacture. Xiang *et al.* investigated the effect of graphite morphology on the corrosion fatigue of ferritic Si–Mo–Al alloys at high temperatures (*i.e.*, 800 °C).^[10] The authors observed that increasing the wall thickness led to undesired graphite morphology, which drastically reduced the corrosion fatigue of the alloy. The literature reports a plethora of studies regarding the corrosion resistance of Si–Mo DI at elevated temperatures as a function of its structure.^[5,6,10–12,24] However, limited data exist regarding the corrosion behavior Si–Mo in aqueous solution. Si–Mo DI components are also subjected to the corrosion effect of the external environment (*e.g.*, rain, humidity, chloride solution, *etc.*). Therefore, the knowledge of the corrosion mechanism of Si–Mo DI in aqueous environments as a function of the cooling rate is very important, which may facilitate the analysis of material loss.

In this work, the effect of the cooling rate controlled by different castings thickness on the mechanical and corrosion properties of Si–Mo spheroidal graphite cast iron was studied. The corrosion behavior was carried out by electrochemical techniques in a 3.5 wt pct NaCl solution at different immersion times. The corroded surface was then analyzed by scanning electron microscopy (SEM) and with energy-dispersive X-ray analysis (EDS) after electrochemical measurements.

II. EXPERIMENTAL METHODS

A. Alloy Preparation

Experimental melts were prepared in a 15-kg-capacity graphite crucible using an electrical induction furnace of an intermediate frequency. The furnace charge consisted of Sorelmetal (high-purity pig iron: 4.46 pct C, 0.132 pct Si, 0.01 pct Mn, 0.006 pct S, and 0.02 pct P), technically pure silica, Fe–Mn, Fe–Mo, and steel scrap. After being melted at 1490 °C, the liquid metal was held for two minutes followed by spheroidization and inoculation operations using the bell method. A Fe–Si–Mg [44 to 46 pct Si; 5.5 to 6.2 pct Mg; 0.8 to 1.2 pct Ca; 0.8 to 1.2 pct RE and Fe (balance)] master alloy was used for the spheroidization, while Fe–Si–Ca–Ba–Al [73 to 78 pct Si, 0.75 to 1.25 pct Ca, 0.75 to 1.25 pct Ba, 0.75 to 1.25 pct Al, and Fe (balance)] alloy was used for inoculation purposes.^[14] The liquid metal was poured at 1360 °C into Y block ingots with plate section sizes of 3, 5, 13, and 25 mm at the bottom end (Figure 1). Sand molds were made using green molding sand consisting of silica sand, bentonite (7 wt pct), a water/bentonite ratio of 0.4, and a granularity of 100 to 200 μm . Moreover, 0.3-mm-diameter thermocouple tips made of Pt/PtRh10 wires located in the geometrical center of each mold cavity were used to measure the real cooling rate close to

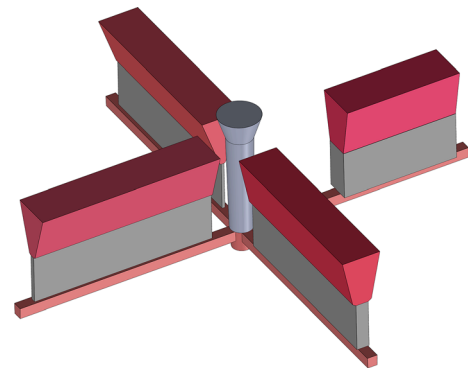


Fig. 1—Outline of test block castings with different wall thicknesses (*i.e.*, 3, 5, 13, and 25 mm).

Table I. Chemical Composition of EN-GJS-SiMo45-6 Alloy (Wt Pct)

C	Si	Mn	Cu	Ni	Cr	Mg	Mo	S	Fe
3.16	4.63	0.18	0.01	0.01	0.02	0.036	0.65	0.01	bal.

equilibrium eutectic temperature ($T_e = 1178$ °C). T_e was determined according to the following equation^[25]:

$$T_e = 1154 + 5.25 \text{ Si} - 14.88 \text{ P}, \quad [1]$$

where Si and P are silicon and phosphorus elements in wt pct, respectively.

The chemical composition tests of the experimental ductile irons were carried out using a SPECTRAMAXx emission spectrometer with spark excitation (Table I).

B. Mechanical Test

Static tensile tests at a constant strain rate were performed using a Zwick Roell AllroundLine Z10 machine that was equipped with a 10-kN load cell (0.5 class) and a dedicated specimen grip (Figure 2). A laserXtens HP1-15 high-precision (0.5 class) speckle-type laser extensometer combined with optical cameras was applied for non-contact strain measurements (strain rate $6.4 \times 10^{-3} \text{ s}^{-1}$). The ultimate tensile strength (R_m), yield strength ($R_{p0.2}$), and elongation (A) were automatically extracted from the recorded curves by dedicated software (ZwickRoell testXpert II). Moreover, Brinell hardness measurements were carried out using an HPO-250 hardness tester.

C. Electrochemical Experiments

The study was carried out on Si–Mo ductile iron with different casting wall thicknesses (*i.e.*, 3, 5, 13, and 25 mm). The samples were inserted in an epoxy resin with a flat surface area of 1 cm^2 . Before each test, the exposed surface was ground with silicon carbide abrasive paper and polished up to 1 μm . The samples were then ultrasonically cleaned with absolute ethanol and

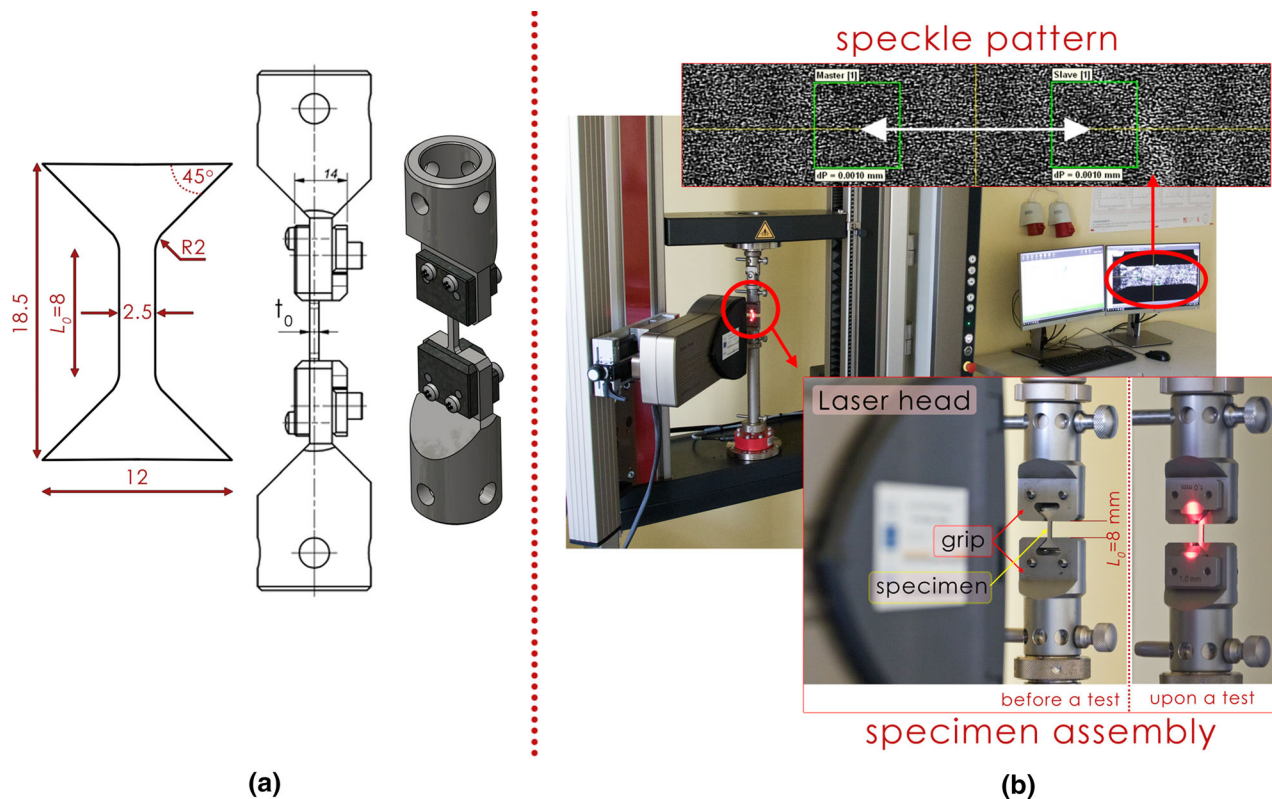


Fig. 2—(a) Tensile specimen shape and dimensions; (b) tensile test specimen assembly.

dried. The electrochemical experiments were performed in a three-electrode cell using a Gamry reference 600 potentiostat/galvanostat electrochemical system that consisted of a platinum foil (*i.e.*, the counter electrode—CE), a saturated calomel electrode (SCE) that was (*i.e.*, reference electrode), and the tested metal that was used as the working electrode. The electrochemical impedance spectroscopy (EIS) tests were recorded at the open-circuit potential (OCP) within a frequency range of 10 kHz to 10 mHz and an amplitude of 10 after prefixed immersion times (*i.e.*, 6, 12, 18, and 24 hours). The EIS results were then simulated with ZSimpWin 3.5 software with the proper electrical equivalent circuit (EEC). The potentiodynamic (PDP) tests were carried out within a range of ± 250 mV vs OCP with a scan rate of 1 mV s^{-1} after maintaining the sample for 24 hours in the tested solution. The corrosion current density (i_{corr}) and the cathodic (β_c) and anodic (β_a) Tafel constants were determined using Echem Analyst 5.21 software. The corrosion rate (CR) was calculated according to ASTM G102 using the following equation^[26]:

$$\text{CR}(\text{mm y}^{-1}) = \frac{3.27 \times 10^{-3} i_{\text{corr}} E_w}{d}, \quad [2]$$

where 3.27×10^{-3} is the conversion factor, i_{corr} is the corrosion current density, E_w is the equivalent weight of the metal, and d is the metal's density. All of the experiments were carried out in a 3.5 wt pct NaCl solution that was prepared from analytical reagent-grade sodium chloride and pure deionized water with an electrical resistivity of $0.055 \mu\text{S cm}^{-1}$ at $T = 25 \pm 1^\circ\text{C}$.

D. Surface Analysis

The tested samples were analyzed using a JEOL JSM-550LV scanning electron microscope and equipped with energy-dispersive X-ray analysis. A Leica MEF 4M microscope and a QWin v3.5 quantitative analyzer were used to carry out the metallographic analysis. To study the ferrite grain size, a Tescan Mira scanning electron microscope that was equipped with an Oxford Electron backscatter diffraction (EBSD) detector was used.

III. RESULTS AND DISCUSSION

A. Microstructure

Figures 3 and 4 show the microstructure and an inverse pole figure (IPF) map of the investigated Si–Mo DI samples, with the morphological details listed in Table II. The SEM micrograph analysis revealed that the microstructure consisted of a ferrite matrix, spheroidal graphite, and minor amounts of island-like pearlite that surrounded the carbide phase (*i.e.*, Fe_2MoC and M_6C) in the intercellular regions.^[1,14] From Table II, it follows that the cooling rate increased exponentially as the casting wall thickness decreased; moreover, it can be seen from Figures 3 and 4 that the cooling rate influenced the microstructure of Si–Mo DI. The graphite nodule count and the ferrite fraction decreased with an increase in cooling rate. The EBSD analysis showed that the ferrite's average grain size also increased from 22.65 to $37.05 \mu\text{m}$ with the changes in

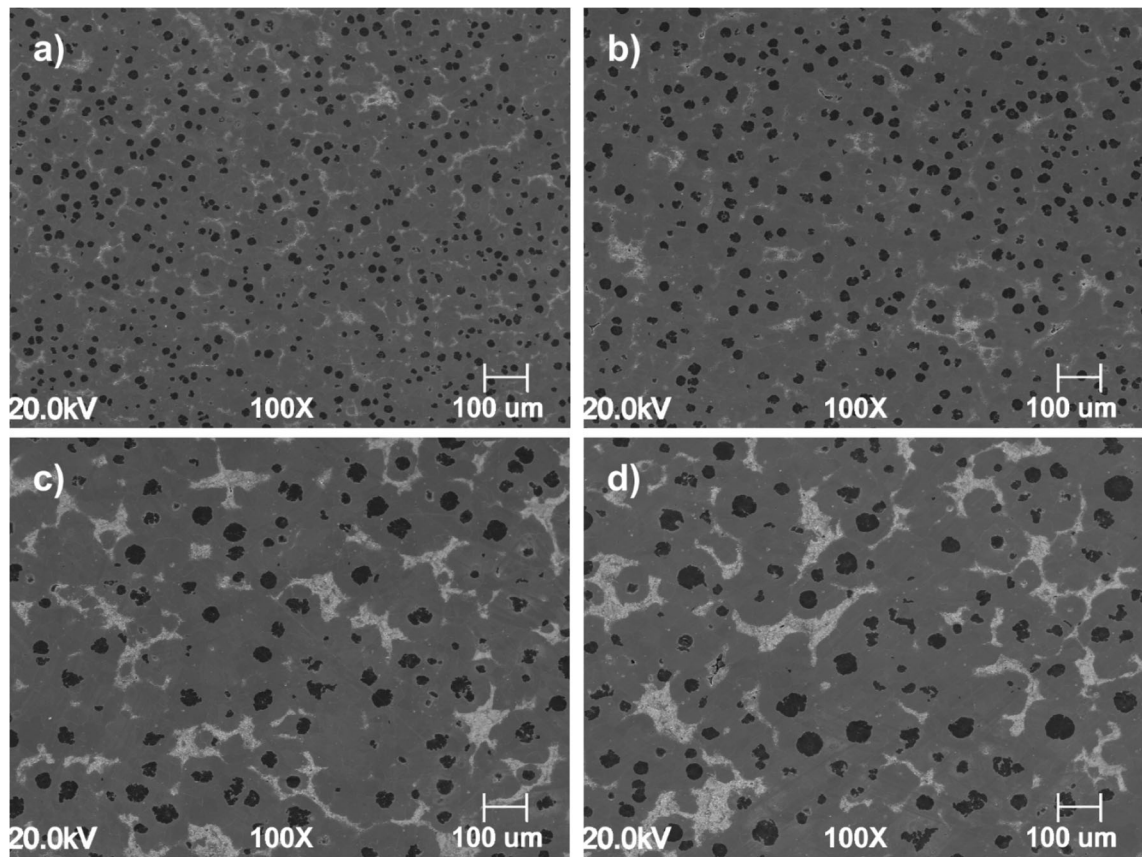


Fig. 3—SEM microstructure of Si-Mo ductile iron: (a) casting No. 1; (b) casting No. 2; (c) casting No. 3; and (d) casting No. 4. Nital-etched samples.

the cooling rate, and the texture of the Si-Mo DI samples was random.

B. Mechanical Properties

Figure 5 shows the effect of the cooling rate on the mechanical properties of the tested samples. It can be observed that the tensile strength (R_m), yield strength ($R_{p0.2}$), and elongation (A) decreased, whereas the hardness increased, as the cooling rate decreased. Among all of the factors, the graphite nodule count and nodularity play a significant role in enhancing the tensile properties of the DI.^[27–32] The high nodularity implies a more regular graphite nodule, which results in fewer stress concentration sites in the graphite–ferrite interface.^[33] These results are in good agreement with those of a previous study; Javaid *et al.*^[34] observed that the mechanical properties of samples with lower casting wall thicknesses increased due to the more homogeneous microstructure (*i.e.*, higher nodule count and graphite nodularity). Moreover, the carbide content also can affect the mechanical properties of the DI alloy. Mohd *et al.*^[32] and Alabbasian *et al.*^[30] reported that DI with a lower carbide content showed better mechanical properties. From the data listed in Table II and Figure 5, it follows that although the cooling rate varies in a broad range (1 to $37\text{ }^{\circ}\text{C s}^{-1}$) when changing the section

thickness from 25 to 3 mm, accompanied by finer microstructure features, the resulting mechanical properties are not fundamentally different from each other. In this connection, the results confirmed the high uniformity of mechanical properties in a wide range of cooling rates between thin-walled and thicker-walled castings.

C. Electrochemical Experiments

1. EIS measurements

Figure 6(a) and (b) shows the Nyquist and Bode plots obtained after 24 hours of immersion in the tested solution for the different cooling rates, respectively. For all of the tested samples, the obtained EIS diagram shows a broad depressed semicircle all over the studied frequencies. The morphological analysis showed that all of the sample surfaces were covered with gray-black and thick red porous corrosion-product layers (Figure 10); therefore, the data that were obtained from the EIS experiments were fitted with an electric equivalent circuit (EEC) with two-time constants, as shown in Figure 6(a) and the fitting parameters are listed in Table III. In this EEC, R_s is the electrolyte resistance, R_f and CPE_f are the resistance and constant phase element of the corrosion products formed after 24 hours of immersion, respectively, while R_{ct} and CPE_{dl} are the

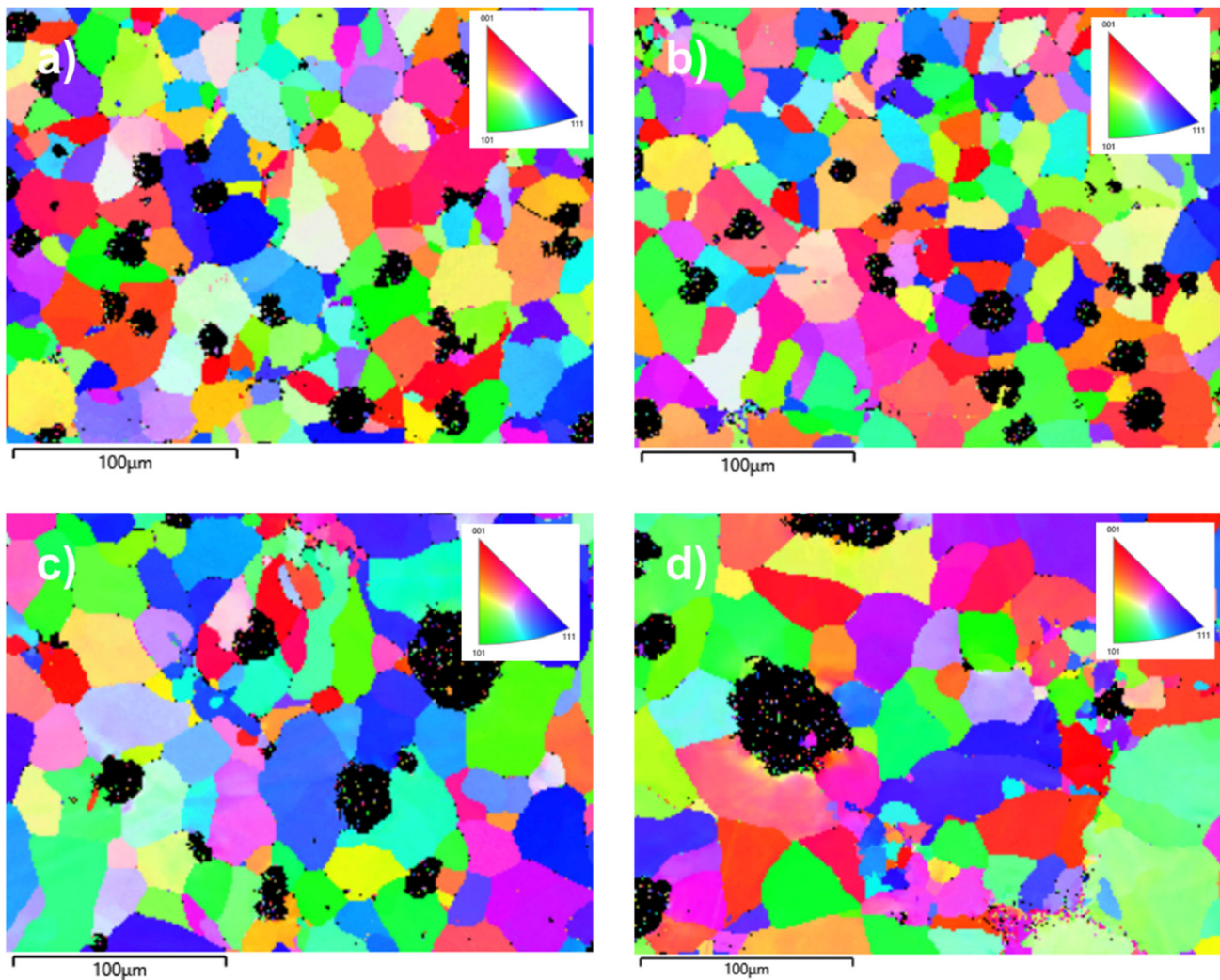


Fig. 4—EBSD Mapping of Si–Mo ductile: (a) casting No. 1; (b) casting No. 2; (c) casting No. 3; and (d) casting No. 4. No etched samples.

Table II. Microstructure Analysis of Si–Mo DI Samples

Casting No.	Wall Thickness (mm)	Cooling Rate ($^{\circ}\text{C s}^{-1}$)	Graphite Nodule Count (mm^{-2})	Graphite Nodularity (Pct)	Ferrite Volume Fraction (Pct)	Ferrite Average Grain Size (μm)
1	3	36.6	608	91	86	22.65
2	5	12.8	411	90	85	25.72
3	13	2.5	201	87	81	34.74
4	25	1.3	168	85	78	37.05

charge transfer resistance and constant phase element representing the double-charge layer capacitance, respectively. It can be seen from Figure 6 that all of the experimental data showed an excellent fit, and the low values of the chi squared (χ^2) are listed in Table III indicating a good fit with the proposed EEC. The value of the polarization resistance can be used to characterize the corrosion resistance of the steel. It is well known that a metal with higher polarization resistance (R_p) shows better corrosion resistance properties. It follows from

the data that the value of R_p decreased after decreasing the cooling rate from 878.10 to 606.39 $\Omega \text{ cm}^2$; therefore, the corrosion resistance of the samples follows this order: 1 > 2 > 3 > 4. The microstructure of Si–Mo ductile iron (DI) is mainly composed of a ferrite metallic matrix (≈ 88 pct), graphite nodules (≈ 10 pct), and a small percentage of segregation in the form of carbides (*i.e.*, Fe_2MoC and M_6C) surrounded by a pearlite island at the intercellular regions (Figure 3). In a multiphase metal, these microstructural components can not only

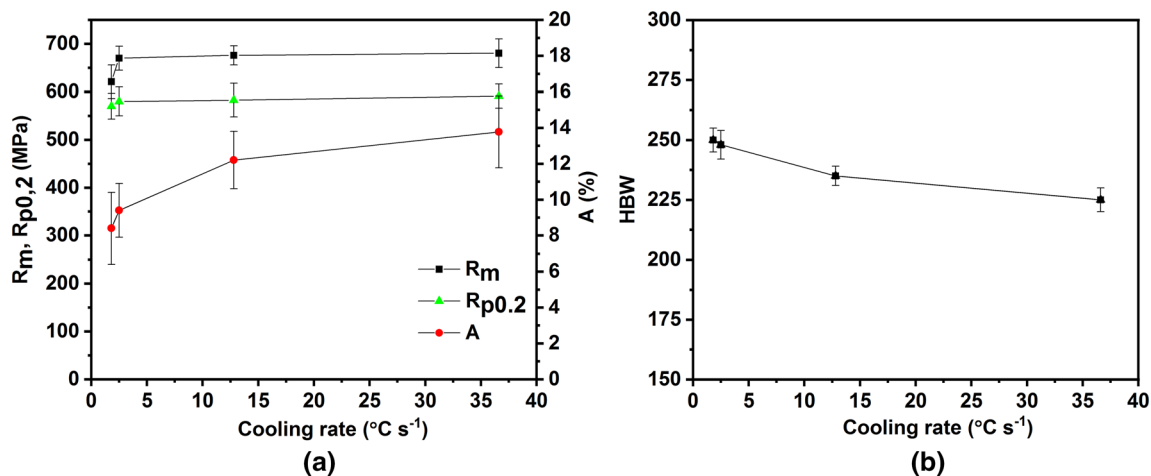


Fig. 5—(a) Tensile, yield strength, and elongation; (b) hardness.

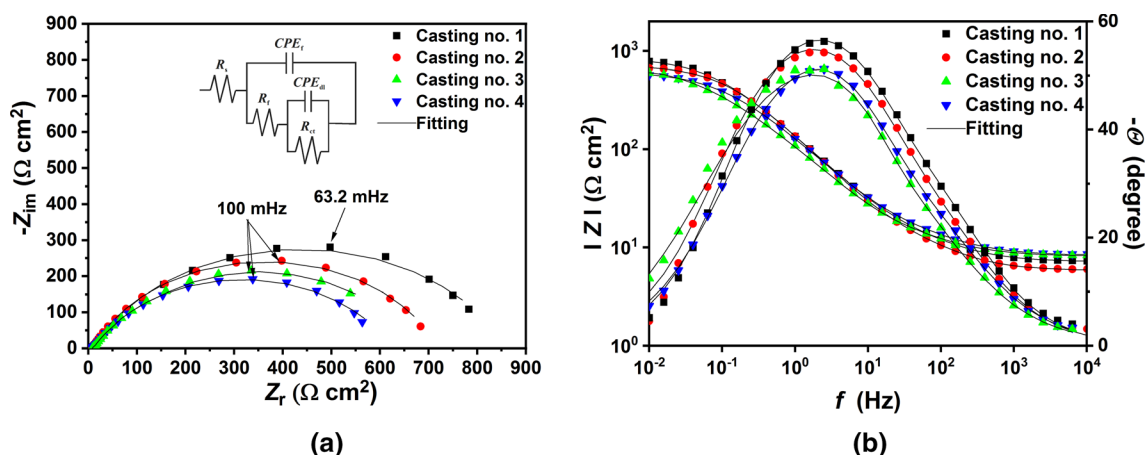


Fig. 6—EIS plots recorded after 24 h of immersion time in a 3.5 pct NaCl solution: (a) Nyquist; (b) Bode.

affect its mechanical properties but also greatly influence its corrosion resistance. The schematic model displayed in Figure 7(a) can be used to describe the micro-corrosion phenomena that occur on a multiphase metal surface. Graphite is nobler than the DI ferrite matrix; thus, the difference in the electrochemical potential establishes micro-galvanic cells at the graphite–matrix interface (Figure 7(b)). The galvanic coupling leads to the preferential dissolution of the matrix around the graphite, leaving voids and a porous mass of corrosion products around the graphite nodule (Figure 7(c)), as shown in the SEM analysis presented in Figure 10. This phenomenon is well known as graphitic corrosion. An analysis of the microstructure showed that, with decreasing the cooling rate, the graphite nodule count decreased, while their sizes increased. However, it is worth mentioning that Górný *et al.*^[14] observed that the average graphite area did not change significantly in a previous study; therefore, it can be speculated that the drop in the corrosion resistance of the steel with decreasing the cooling rate should not be attributed to this phenomenon. On the other hand, the carbide fraction increased when the cooling rate decreased.

The iron carbide that is present in the pearlite phase is less active than the ferrite phase; thus, the latter phase acts like an anode, and the former behaves like a cathode.^[23] Furthermore, the galvanic effect between the lamellar ferrite and the lamellar cementite in the pearlite phase is stronger than that between the lamellar cementite and the pro-eutectoid ferrite region; therefore, the anodic dissolution rate of the lamellar ferrite is faster than that of the pro-eutectoid ferrite region.^[20,21] After the preferential dissolution of the lamellar ferrite, a stable residual cementite region accumulates on the metal surface, thus, increasing the cathodic area, which in turn enhances the galvanic effect^[20,21] and further accelerates the dissolution of the metal.^[23]

An analysis of the microstructure of the tested samples (Table II) also revealed as the cooling rate decreased, the ferrite's average grain size increased. The EIS results suggest that the corrosion resistance of the Si–Mo DI samples decreased along with an increase in the grain size. Similar results have also been reported in the literature for steel alloys in a 3.5 wt pct NaCl solution. It is well known that grain boundary regions have higher electrochemical activity as compared to the

Table III. EIS Parameters of Samples After 24 h of Immersion

Casting No.	Immersion Time (h)	CPE _f			CPE _{dl}			R_{ct} (Ω cm ²)	$R_p = R_f + R_{ct}$ (Ω cm ²)	χ^2 (10 ⁻⁴)
		R_s (Ω cm ²)	Q_f (m Ω^{-1} s ⁿ cm ⁻²)	n_f	R_f (Ω cm ²)	Q_{dl} (m Ω^{-1} s ⁿ cm ⁻²)	n_{dl}			
1	6	7.38	0.69	0.79	10.25	0.93	0.78	884.70	894.95	4.87
	12	7.28	0.81	0.76	13.96	0.93	0.74	842.70	856.66	4.99
	18	7.20	0.93	0.74	15.13	0.81	0.73	847.60	862.73	3.59
	24	7.13	1.02	0.74	17.80	0.86	0.72	836.30	878.10	4.25
2	6	6.22	1.15	0.76	11.60	1.12	0.74	751.50	763.10	4.95
	12	5.99	1.03	0.76	14.59	1.04	0.74	753.80	768.39	3.36
	18	5.93	0.98	0.75	16.73	0.86	0.75	735.90	752.63	2.44
	24	5.85	0.95	0.76	17.59	0.82	0.75	705.10	722.69	3.03
3	6	8.47	1.39	0.69	14.49	0.55	0.78	684.50	698.99	3.56
	12	8.26	1.66	0.68	16.33	0.63	0.75	714.90	731.23	3.95
	18	8.11	2.31	0.65	20.30	0.31	0.75	689.40	709.07	3.23
	24	8.01	2.62	0.64	23.65	0.56	0.74	651.11	674.76	5.84
4	6	8.42	1.15	0.69	35.22	0.33	0.82	601.90	637.12	6.46
	12	8.32	1.40	0.68	26.18	0.52	0.82	640.90	667.08	2.27
	18	8.48	1.64	0.69	30.25	0.41	0.83	622.90	653.15	3.83
	24	8.21	1.56	0.67	30.65	0.49	0.79	588.70	619.35	3.28

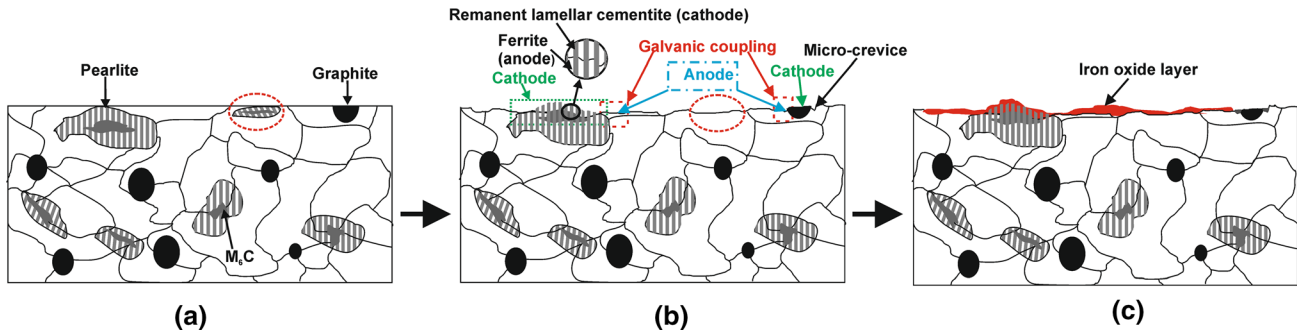


Fig. 7—Schematic model of anodic and cathodic interactions of Si-Mo ductile iron. (a) polished metal; (b) micro-galvanic cells; (c) preferential dissolution of the matrix.

inside part of the grain.^[35–38] The volume fraction of the grain boundaries increases with grain refinement; as a result, grain-grain boundary micro-galvanic cells are formed all over the metal surface. The even distribution of these micro-galvanic cells on the metal surface promotes the nucleation of the inner corrosion-product layer, which in turn prevents the aggressive solution from reaching the metal surface. However, it is worth mentioning that if on one hand, the Hall–Petch equation well describes the correlation between the mechanical properties and grain size of the steel, on the other hand, the relationship between the corrosion behavior and the grain size of the steel is not so straightforward. There seems to be no unanimous consensus regarding the effect of grain size on the corrosion of steel alloys. Some studies have also reported that, in a 3.5 wt pct NaCl solution, finer grains tend to decrease the corrosion resistance of steel alloys.^[39–41] Nevertheless, the variation of grain size with the cooling rate is also an important factor that must take into account, which can also contribute to influencing the corrosion behavior of tested samples.

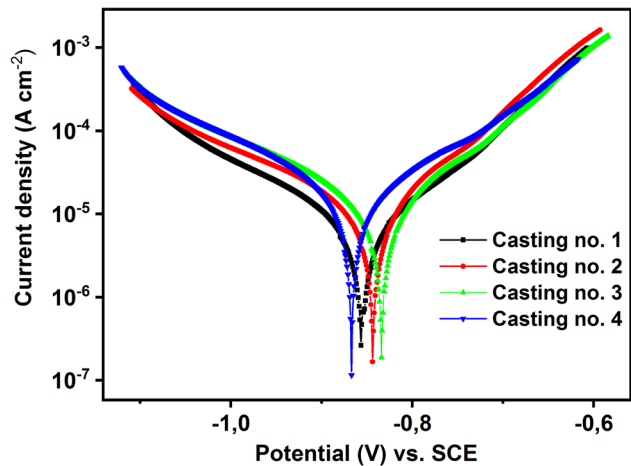


Fig. 8—Potentiodynamic polarization curves after 24 h of immersion in a 3.5 pct NaCl solution.

2. PDP measurements

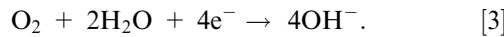
Figure 8 and Table IV show the potentiodynamic polarization measurements and the corresponding

Table IV. Corrosion Parameters of Si–Mo DI Samples Recorded After 24 h of Immersion in a 3.5 pct NaCl Solution

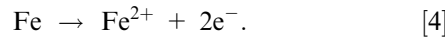
Casting No.	E_{corr} (V)	β_c (V dec ⁻¹)	β_a (V dec ⁻¹)	i_{corr} ($\mu\text{A cm}^{-2}$)	CR (mm y ⁻¹)
1	– 0.856	0.183	0.122	7.36	0.09
2	– 0.843	0.218	0.139	12.47	0.15
3	– 0.834	0.211	0.150	15.60	0.19
4	– 0.867	0.210	0.169	18.89	0.23

corrosion kinetic parameters observed after 24 hours of immersion in the tested solution, respectively. It follows from the data that the corrosion current density increased with decreasing the cooling rate. As the fraction of the pearlite-carbide phase increased, the number of micro-galvanic cells also increased, making the DI more active thermodynamically. Furthermore, the cathodic and anodic current densities varied with the cooling rate. The cathodic (β_c) and anodic (β_a) Tafel slopes of the DI increased from 0.180 to 0.210 V dec⁻¹ and 0.122 to 0.169 V dec⁻¹, respectively, with decreasing cooling rate. These results suggest that there was a change in the rate-determining step from a charge transfer to a combination of a charge transfer and a limit diffusion step^[20–22,42] with an increase in the pearlite-carbide fraction.

In an aerated solution, the cathodic reaction of steel is characterized by the reduction of oxygen:



The anodic reaction is characterized by the dissolution of the ferrite phase.



With the dissolution of the lamellar ferrite, the narrow gap left between the lamellar cementite inhibits the diffusion of O_2 and Fe^{2+} ions that are moving toward or away from the metal surface,^[20,21] thus, changing the rate-determining step. The corrosion rate of the samples calculated with Eq. [2] follows this order: $4 > 3 > 2 > 1$, which is in agreement with the EIS results.

3. Effect of time

The Nyquist and Bode plots of the tested samples carried out after different immersion times (*e.g.*, 6, 12, 18, and 24 hours) in a 3.5 wt pct NaCl solution are shown in Figure 9. The EIS data were fitted with the EEC shown in Figure 6(a), and the fitting parameters as a function of the immersion time are listed in Table III. It can be seen from the Nyquist and Bode plots that all of the Si–Mo DI samples exhibited a similar depressed capacitive loop with little differences in the diameters of the capacitive arc and impedance modulus at 0.01 Hz ($Z_{0.01 \text{ Hz}}$). It follows from the data that the values of R_{ct} slightly decreased with increased immersion times. These results indicate that the corrosion mechanism did not change over time and that all of the DI steels were characterized by good corrosion resistance after long immersion times. The n_{dl} exponent also decreased

slightly after prolonged immersion times. The n exponent in CPE is a measure of the surface homogeneity of the metal^[43]; Therefore, the change of this parameter indicated a certain increase in the surface roughness. This observation is in agreement with the SEM analysis presented in Figure 10.

D. Surface Analysis

An SEM analysis of the Si–Mo DI samples after 24 hours of immersion in a 3.5 wt pct NaCl solution is shown in Figure 10. After 24 hours of immersion, all of the surface samples were covered by a thick and uneven red porous corrosion-product layer (Figures 10(a') through (d')), which was mainly composed of iron oxide and NaCl, as revealed by the EDS analysis listed in Table V. The presence of NaCl can be ascribed to the residual corrosion solution. Moreover, this layer was loosely adherent to the DI surface and was easy to remove. Figure 10(a) through (d) shows the DI sample's surface after removing the corrosion-product layer. It can be observed that all of the DI samples showed homogenous corrosion, with a selective attack around the graphite nodules due to the graphitic corrosion. The attack formed microcrevices around the graphite nodules (Figure 11(a)), thus, leaving a mass of corrosion products (*i.e.*, mainly iron oxide) and a carbon powder layer that surrounded the nodules. Moreover, the figures show the remaining lamellar cementite structure and the island-like carbide phase protruding from the DI surface (Figure 11(b)), resulting from the dissolution of lamellar ferrite in the perlite and the adjacent ferrite phase matrix. As the immersion time increased, the lamellar cementite gradually accumulated on the metal surface.^[20,21] Furthermore, even though detachment of the lamellar cementite adjacent ferrite phase matrix is difficult, it is also possible that some cementite might have fallen off from the matrix to the solution^[21] (*e.g.*, the red lines that are shown in Figures 7(a) and (b)) and precipitated on the DI surface. The EDS analysis (the red square in Figure 10) showed the presence of Fe, C, Na, and other alloying elements of the DI steel's surface, which might have been due to the accumulation of residual Fe_3C and the corrosion solution.

IV. CONCLUSIONS

The effect of the cooling rate on the mechanical and corrosion properties of Si–Mo ductile cast iron was investigated in this paper. The findings can be summarized as follows:

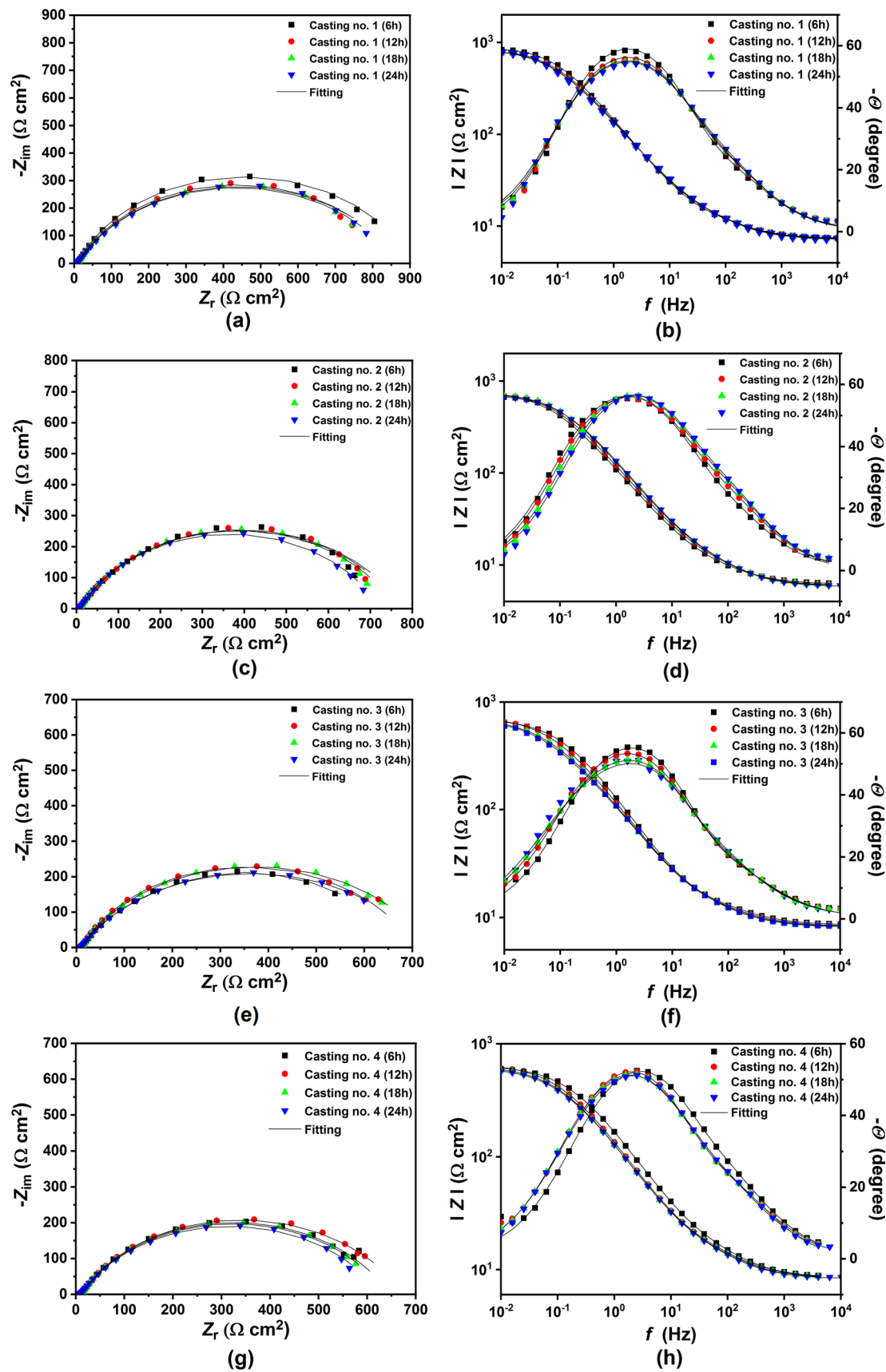


Fig. 9—EIS plots for tested steels as a function of immersion times. (a, b) casting No. 1; (c, d) casting No. 2; (e, f) casting No. 3; and (g, h) casting No. 4.

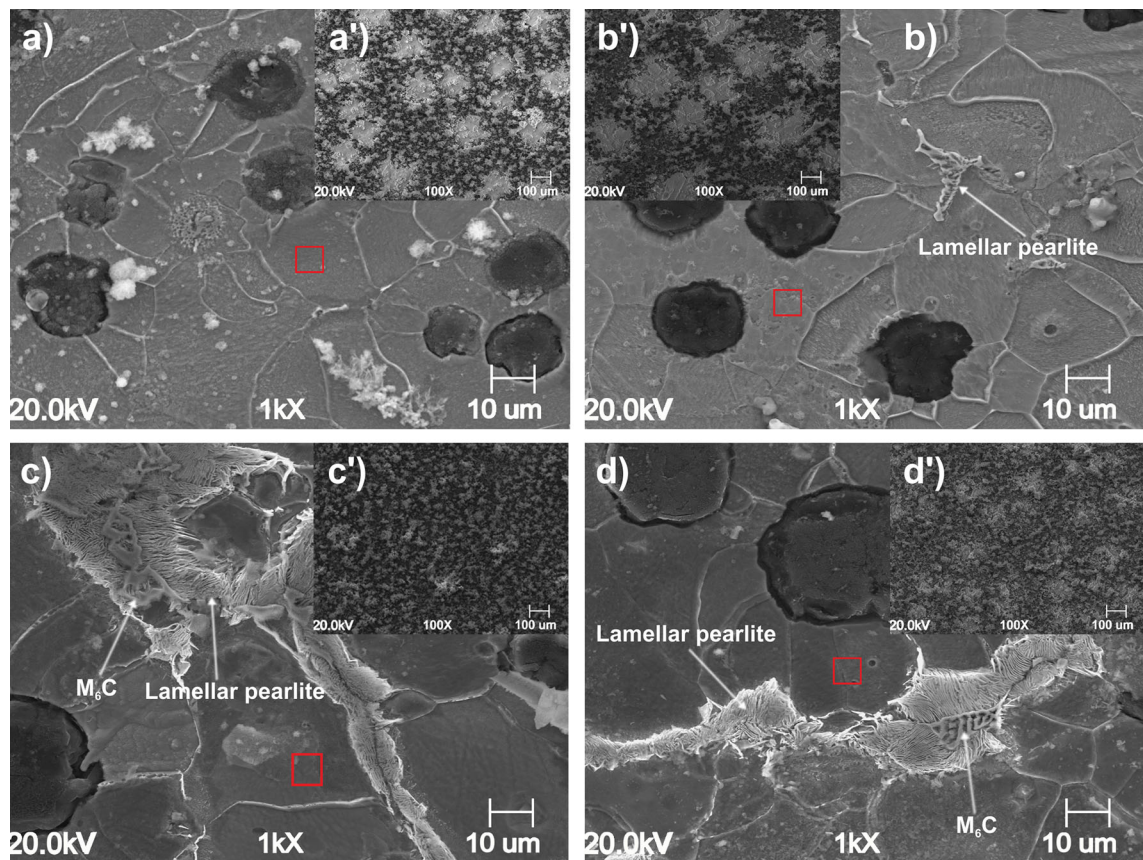


Fig. 10—SEM analysis after 24 h of immersion in a 3.5 wt pct solution: (a') casting no. 1; (b') casting no. 2; (c') casting no. 3 and (d') casting no. 4 (with loosely adherent corrosion products). (a) casting no. 1; (b) casting no. 2; (c) casting no. 3 mm; and (d) casting no. 3 (after washing).

Table V. EDS analysis Carried Out After 24 h of Immersion

Casting No.	C	O	Si	Mn	Ni	Mo	Na	Cl	Fe
Porous Layer									
1	—	13.21	1.31	0.05	0.08	0.25	1.54	4.74	78.82
2	—	12.45	1.45	0.14	0.05	0.15	1.58	4.55	79.63
3	0.31	16.50	1.17	0.24	0.08	0.16	1.53	3.16	76.85
4	0.61	12.43	2.16	0.08	0.07	0.17	1.61	4.48	78.39
Metal Surface									
1	1.80	1.10	4.53	0.23	0.29	0.37	0.42	—	91.27
2	1.67	2.57	4.20	0.21	0.12	0.76	1.32	—	89.15
3	2.44	1.63	3.83	0.05	0.40	0.51	0.74	—	93.40
4	2.42	1.66	5.18	0.08	0.09	0.64	0.34	—	89.59
Micro-crevice	13.92	7.11	3.12	0.35	0.19	0.18	5.48	—	69.65

- (a) An SEM-EBSD analysis showed that an increase in the cooling rate led to a more homogeneous structure and increased the tensile properties of the Si-Mo DI.
- (b) The electrochemical results showed that the corrosion resistance of the DI steel decreased with decreases in the cooling rate. The results revealed that the difference in corrosion resistance could have been attributed to the increase in pearlite-carbide segregation fraction while

decreasing the cooling rate due to the galvanic effect between the nobler cementite phase and the ferrite phase. Moreover, the electrochemical results carried out at different immersion times showed that the corrosion rate of the DI steels only slightly increased with longer immersion times; this indicated that the DI steels were characterized by good corrosion stability over time.

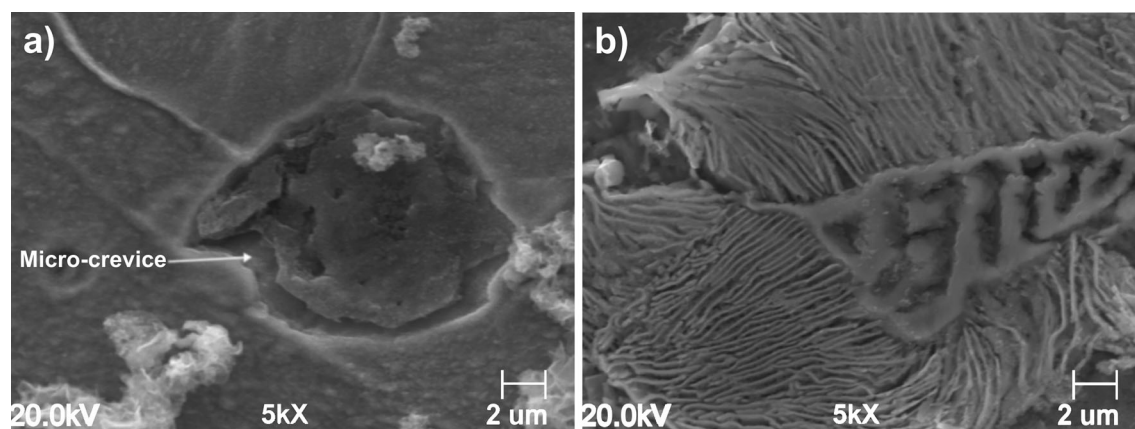


Fig. 11—(a) Micro-crevice generated after graphitic corrosion; (b) carbide phase surrounded by lamellar pearlite.

- (c) EBSD microstructure analysis revealed that the ferrite grain size increased with decreases in the cooling rate, which could have also contributed to influencing the corrosion behavior of the tested samples.
- (d) SEM analysis revealed that, after 24 hours of immersion, the DI steels were covered by a thick and uneven red porous corrosion-product layer that was mainly composed of iron oxide loosely adhered to the metal surface. Furthermore, all of the DI samples showed homogenous corrosion, with selective attacks around the graphite nodules and the remaining island-like lamellar cementite structure.

ACKNOWLEDGMENTS

The research was supported by AGH Research Project No. 16.16.170.654.

CONFLICT OF INTEREST

The authors declare no conflict of interest.

OPEN ACCESS

This article is licensed under a Creative Commons Attribution 4.0 International License, which permits use, sharing, adaptation, distribution and reproduction in any medium or format, as long as you give appropriate credit to the original author(s) and the source, provide a link to the Creative Commons licence, and indicate if changes were made. The images or other third party material in this article are included in the article's Creative Commons licence, unless indicated otherwise in a credit line to the material. If material is not included in the article's Creative Commons licence and your intended use is not permitted by statutory regulation or exceeds the permitted use, you will need

to obtain permission directly from the copyright holder. To view a copy of this licence, visit <http://creativecommons.org/licenses/by/4.0/>.

REFERENCES

1. B. Black, G. Burger, R. Logan, R. Perrin, and R. Gundlach: *SAE Technical Paper 2002-01-2115*, 2002, vol. 111, pp. 976–91. <https://doi.org/10.4271/2002-01-2115>.
2. EN 16124, Founding Low-Alloyed Ferritic Spheroidal Graphite Cast Irons for Elevated Temperature Applications, 2011.
3. P. Matteis, G. Scavino, A. Castello, and D. Firrao: *Procedia Mater. Sci.*, 2014, vol. 3, pp. 2154–59. <https://doi.org/10.1016/j.mspro.2014.06.349>.
4. D. Pierce, A. Haynes, J. Hughes, R. Graves, P. Maziasz, G. Muralidharan, A. Shyam, B. Wang, R. England, and C. Daniel: *Prog. Mater. Sci.*, 2019, vol. 103, pp. 109–79. <https://doi.org/10.1016/j.pmatsci.2018.10.004>.
5. S. Xiang, S. Jonsson, P. Hedström, B. Zhu, and J. Odqvist: *Int. J. Fatigue*, 2021, vol. 143, p. 105984. <https://doi.org/10.1016/j.ijfatigue.2020.105984>.
6. K.H. Choe, S.M. Lee, and K.W. Lee: *Mater. Sci. Forum*, 2010, vol. 654–656, pp. 542–45. <https://doi.org/10.4028/www.scientific.net/MSF.654-656.542>.
7. D. Li, R. Perrin, G. Burger, D. McFarlan, B. Black, R. Logan, and R. Williams: *SAE Technical Paper 2004-01-0792*, 2004. <http://doi.org/10.4271/2004-01-0792>.
8. S. Xiang, Oxidation, Creep and Fatigue Synergies in Cast Materials for Exhaust Manifolds. KTH Royal Institute of Technology, 2021.
9. K. L. Choe, K.; Kim, M. In Proceedings of the International Conference on Materials; Environmental and Biological Engineering (MEBE 2015), Guilin, China, 2015.
10. S. Xiang, P. Hedström, B. Zhu, J. Linder, and J. Odqvist: *Int. J. Fatigue*, 2020, vol. 140, p. 105781. <https://doi.org/10.1016/j.ijfatigue.2020.105781>.
11. M. Stawarz and P.M. Nuckowski: *Materials*, 2020, vol. 13, p. 1745. <https://doi.org/10.3390/ma13071745>.
12. S.N. Lekakh, A. Bofah, R. Osei, R. O'Malley, L. Godlewski, and M. Li: *Oxid. Met.*, 2021, vol. 95, pp. 251–68. <https://doi.org/10.1007/s11085-021-10022-1>.
13. A.D. Sosa, M.D. Echeverría, O.J. Moncada, N. Míngolo, and J.A. Sikora: *J. Mater. Process. Technol.*, 2009, vol. 209, pp. 5545–51. <https://doi.org/10.1016/j.jmatprotec.2009.05.010>.
14. M. Górny, M. Kawalec, B. Gracz, and M. Tupaj: *Metals*, 2021, vol. 11, p. 1634. <https://doi.org/10.3390/met11101634>.
15. K.M. Ibrahim and Y. Fouad: *Int. J. Cast Met. Res.*, 2013, vol. 26, pp. 184–91. <https://doi.org/10.1179/1743133613Y.0000000056>.

16. M. Górny and M. Kawalec: *J. Mater. Eng. Perform.*, 2013, vol. 22, pp. 1519–24. <https://doi.org/10.1007/s11665-012-0432-8>.
17. M. Youssef, A. Nofal, and A. Hussein: *Mater. Sci. Forum*, 2018, vol. 925, pp. 231–38. <https://doi.org/10.4028/www.scientific.net/MSF.925.231>.
18. G. Angella, R. Donnini, D. Ripamonti, M. Górny, and F. Zanardi: *Metals*, 2019, vol. 9, p. 1019. <https://doi.org/10.3390/met9091019>.
19. M. Benedetti, V. Fontanari, and D. Lusuardi: *Eng. Fract. Mech.*, 2019, vol. 206, pp. 427–41. <https://doi.org/10.1016/j.engfractmech.2018.12.019>.
20. X. Hao, J. Dong, I.-I.N. Etim, J. Wei, and W. Ke: *Corros. Sci.*, 2016, vol. 110, pp. 296–304. <https://doi.org/10.1016/j.corsci.2016.04.042>.
21. X. Hao, X. Zhao, H. Chen, B. Huang, J. Ma, C. Wang, and Y. Yang: *J. Mater. Res. Technol.*, 2021, vol. 12, pp. 399–411. <https://doi.org/10.1016/j.jmrt.2021.02.095>.
22. J. Wei, Y. Zhou, J. Dong, X. He, and W. Ke: *Materialia*, 2019, vol. 6, p. 100316. <https://doi.org/10.1016/j.mtla.2019.100316>.
23. G. Palumbo, M. Górny, and J. Banaś: *J. Mater. Eng. Perform.*, 2019, vol. 28, pp. 6458–70. <https://doi.org/10.1007/s11665-019-04379-3>.
24. S.N. Lekakh, A. Bofah, L.A. Godlewski, and M. Li: *Metals*, 2022, vol. 12, p. 66. <https://doi.org/10.3390/met12040661>.
25. F. Neuman: The influence of additional elements on the physic-chemical behaviour of carbon in saturated molten iron, in *Recent Research on Cast Iron*. H.D. Merchant, ed., Gordon and Breach, New York, 1968, pp. 659–703.
26. ASTM-G102, Standard Practice for Calculation of Corrosion Rates and Related Information from Electrochemical Measurements, 1994.
27. M.A. Sheikh and J. Iqbal: *J. Rare Earths*, 2007, vol. 25, pp. 533–36. [https://doi.org/10.1016/S1002-0721\(07\)60557-2](https://doi.org/10.1016/S1002-0721(07)60557-2).
28. J.O. Choi, J.Y. Kim, C.O. Choi, J.K. Kim, and P.K. Rohatgi: *Mater. Sci. Eng. A*, 2004, vol. 383, pp. 323–33. <https://doi.org/10.1016/j.msea.2004.04.060>.
29. A. De Santis, O. Di Bartolomeo, D. Iacoviello, and F. Iacoviello: *J. Mater. Process. Technol.*, 2008, vol. 196, pp. 292–302. <https://doi.org/10.1016/j.jmatprotec.2007.05.056>.
30. F. Alabbasian, S.M.A. Boutorabi, and S. Kheirandish: *Mater. Sci. Eng. A*, 2016, vol. 651, pp. 467–73. <https://doi.org/10.1016/j.msea.2015.09.024>.
31. R. Ghasemi, J. Olofsson, A.E.W. Jarfors, and I.L. Svensson: *Int. J. Cast. Met. Res.*, 2017, vol. 30, pp. 125–32. <https://doi.org/10.1080/13640461.2016.1261520>.
32. M. Mohd Rashidi and M.H. Idris: *Mater. Des.*, 2013, vol. 51, pp. 861–69. <https://doi.org/10.1016/j.matdes.2013.04.064>.
33. Z.-H. Wang, X. Zhang, F.-L. Xu, K.-C. Qian, and K.-M. Chen: *China Foundry*, 2019, vol. 16, pp. 386–92. <https://doi.org/10.1007/s41230-019-9080-z>.
34. A. Javaid, J. Thomson, K.G. Davis, and M. Sahoo: *Trans. Am. Foundry Soc.*, 2001, vol. 109, pp. 1–18.
35. A.A. Tiamiyu, U. Eduok, J.A. Szpunar, and A.G. Odeshi: *Sci. Rep.*, 2019, vol. 9, p. 12116. <https://doi.org/10.1038/s41598-019-48594-3>.
36. Q. Yang, Y. Zhou, Z. Li, and D. Mao: *Materials*, 2019, vol. 12, p. 1455. <https://doi.org/10.3390/ma12091455>.
37. H.B. Li, Z.H. Jiang, Q.F. Ma, and Z. Li: *Adv. Mater. Res.*, 2011, vol. 217–218, pp. 1180–84. <https://doi.org/10.4028/www.scientific.net/AMR.217-218.1180>.
38. L. Onyeji and G. Kale: *J. Mater. Eng. Perform.*, 2017, vol. 26, pp. 5741–52. <https://doi.org/10.1007/s11665-017-3031-x>.
39. P. Wang, L. Ma, X. Cheng, and X. Li: *J. Alloys Compds.*, 2021, vol. 857, p. 158258. <https://doi.org/10.1016/j.jallcom.2020.158258>.
40. A.H. Seikh: *J. Chem.*, 2013, vol. 2013, p. 587514. <https://doi.org/10.1155/2013/587514>.
41. M. Soleimani, H. Mirzadeh, and C. Dehghanian: *Mater. Res. Express*, 2020, vol. 7, p. 016522. <https://doi.org/10.1088/2053-1591/ab62fa>.
42. J.B. Sun, G.A. Zhang, W. Liu, and M.X. Lu: *Corros. Sci.*, 2012, vol. 57, pp. 131–38. <https://doi.org/10.1016/j.corsci.2011.12.025>.
43. H. Luo, C.F. Dong, X.Q. Cheng, K. Xiao, and X.G. Li: *J. Mater. Eng. Perform.*, 2012, vol. 21, pp. 1283–91. <https://doi.org/10.1007/s11665-011-0030-1>.

Publisher's Note Springer Nature remains neutral with regard to jurisdictional claims in published maps and institutional affiliations.